



RESEARCH LETTER

10.1002/2017GL073019

Special Section:

Early Results: Juno at Jupiter

Key Points:

- A high correlation between visibly dark clouds and 5-micron radiation extends only partially to microwave radiation
- Five-micron spectroscopy and microwave radiometry yield a 5-bar NH_3 abundance not inconsistent with Galileo results
- Meridional dependence of deep atmospheric opacity is dynamically consistent with most other vertical-motion tracers

Correspondence to:

G. S. Orton,
glenn.orton@jpl.nasa.gov

Citation:


Orton, G. S., et al. (2017), Multiple-wavelength sensing of Jupiter during the Juno mission's first perijove passage, *Geophys. Res. Lett.*, *44*, doi:10.1002/2017GL073019.

Received 10 FEB 2017
Accepted 9 MAR 2017

©2017. California Institute of Technology. Government sponsorship acknowledged.

This Contribution was produced by members of the Jet Propulsion Laboratory, California Institute of Technology and is considered a work-for-hire. In accordance with the contract between the California Institute of Technology and the National Aeronautics and Space Administration, the United States Government and others acting on its behalf shall have, for Governmental purposes, a royalty-free, nonexclusive, irrevocable, world-wide license to publish, distribute, copy, exhibit and perform the work, in whole or in part, to authorize others to do so, to reproduce the final published and/or electronic form of the Contribution, to include the work on the NASA/JPL Technical Reports Server web site, and to prepare derivative works including, but not limited to, abstracts, lectures, lecture notes, press releases, reviews, textbooks, reprint books, and translations.

Multiple-wavelength sensing of Jupiter during the Juno mission's first perijove passage

G. S. Orton¹ , T. Momary¹ , A. P. Ingersoll² , A. Adriani³ , C. J. Hansen⁴ , M. Janssen¹ , J. Arballo¹, S. K. Atreya⁴, S. Bolton⁵ , S. Brown¹, M. Caplinger⁶, D. Grassi³ , C. Li¹, S. Levin¹ , M. L. Moriconi^{3,7}, A. Mura³ , and G. Sindoni³ 

¹Jet Propulsion Laboratory, California Institute of Technology, Pasadena, California, USA, ²Division of Geological and Planetary Sciences, California Institute of Technology, Pasadena, California, USA, ³INAF-Istituto di Astrofisica e Planetologia Spaziali, Rome, Italy, ⁴Planetary Science Laboratory, University of Michigan, Ann Arbor, Michigan, USA, ⁵Southwest Research Institute, San Antonio, Texas, USA, ⁶Malin Space Science Systems, San Diego, California, USA, ⁷CNR-Istituto di Scienze dell'Atmosfera e del Clima, Rome, Italy

Abstract We compare Jupiter observations made around 27 August 2016 by Juno's JunoCam, Jovian Infrared Auroral Mapper (JIRAM), MicroWave Radiometer (MWR) instruments, and NASA's Infrared Telescope Facility. Visibly dark regions are highly correlated with bright areas at $5\ \mu\text{m}$, a wavelength sensitive to gaseous NH_3 gas and particulate opacity at $p \leq 5$ bars. A general correlation between $5\text{-}\mu\text{m}$ and microwave radiances arises from a similar dependence on NH_3 opacity. Significant exceptions are present and probably arise from additional particulate opacity at $5\ \mu\text{m}$. JIRAM spectroscopy and the MWR derive consistent 5-bar NH_3 abundances that are within the lower bounds of Galileo measurement uncertainties. Vigorous upward vertical transport near the equator is likely responsible for high NH_3 abundances and with enhanced abundances of some disequilibrium species used as indirect indicators of vertical motions.

Plain Language Summary Comparison of observations of Jupiter by different Juno and ground-based instruments verified some long-standing relationships, such as those between visibly dark regions and clear, dry parts of the atmosphere. But Juno saw significant exceptions. Different instrument results for the abundance of ammonia gas, a condensate similar to water in the Earth's atmosphere, at 5 bars of pressure were self-consistent and within the uncertainty of Galileo results. The substantial upwelling of ammonia detected by the Microwave Radiometer from great depth near the equator is consistent with other indirect tracers of vertical winds.

1. Introduction

We compare remote-sensing measurements from Juno's first close approach to Jupiter when in orbit, known as "perijove 1" (or PJ1) on 27 August 2016. This comparison addresses correlations between cloud colors and depths, differentiation of opacity sources, and the implications of condensates and disequilibrium species for the dynamics of the atmosphere. Taken altogether, these provide a deeper level of insight into the extent of coupling between different atmospheric levels.

2. Materials and Methods

We present observations of Jupiter made by three of Juno's remote-sensing instruments: JunoCam, the education/public-outreach camera; the Jovian Infrared Auroral Mapper (JIRAM); and the MicroWave Radiometer (MWR), together with contemporaneous ground-based near-infrared images from NASA's Infrared Telescope Facility (IRTF). We select observations with overlapping coverage of $60^\circ\text{--}130^\circ\text{W}$ and $70^\circ\text{S--}70^\circ\text{N}$ (Figure 1). First, we validate relationships between visible cloud color and cloud depth established by previous spacecraft and Earth-based measurements. We compare retrievals of gaseous NH_3 abundances from the JIRAM and MWR observations in the upper troposphere, and we compare MWR measurements of opacity much deeper in the atmosphere and their implications for vertical transport with other indirect measures of vertical motion from previous spacecraft and Earth-based measurements.

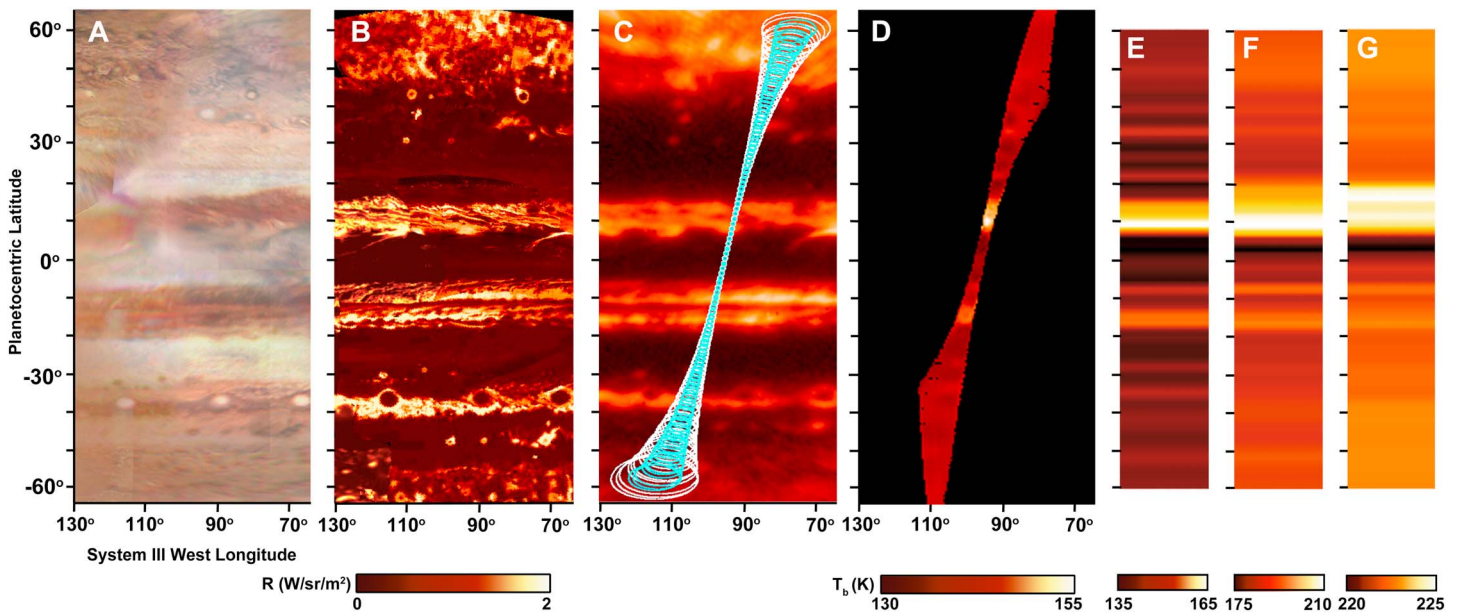


Figure 1. Comparison of different observations of the same region of Jupiter near PJ1, represented by cylindrical projections. (a) Color composite of JunoCam images. (b) High-resolution JIRAM 5- μm map covering most of this region, supplemented by a lower-resolution global map. (c) A 5.1- μm map from an image obtained at NASA's Infrared Telescope Facility ~ 2 h before perijove (27 August 2016, at 1:18 UT), verifying the forward projection in time of the JIRAM 5- μm observations to the perijove epoch. Figure 1c also illustrates several full width at half power “footprints” for MWR channel 6 (blue) and channel 1 (white). (d) Map of MWR brightness temperatures in channel 6 (1.37 cm). (e–g) The meridional variability of zonally averaged brightness temperature in MWR channels 6, 5 (3.0 cm), and 4 (5.75 cm), respectively. Figures 1e–1g are illustrated as extended horizontally to simulate zonal-mean values.

3. Detailed Description of the Data

3.1. JunoCam

Color images were constructed from images of Jupiter in red, green, and blue filters by JunoCam [Hansen et al., 2014]. Figure 1a shows a mosaic of map-projected JunoCam images that include both “close-up” images taken within 2 h of perijove passage and those taken as a part of inbound and outbound sequences. The images used to compare with the regions of the atmosphere covered by JIRAM and the MWR include files 6151, 6159, 6160, and 6180, with some inputs from files 6171, 6174, and 6186 (using shortened versions of original file names: JNCE_2016240_00C06151_V01, etc.). The spatial resolution on Jupiter ranged from tens to hundreds of kilometers.

3.2. JIRAM

A series of maps of Jupiter's radiance was made by using JIRAM's 5- μm filtered camera [Adriani et al., 2014]. The highest resolution maps were combined in a mosaic covering the track of MWR observations ~ 5 h before perijove with a mean spatial resolution of 110 km (Figure 1b). A global map was created from observations obtained at greater distances from Jupiter. The JIRAM spatial resolutions of the maps used in Figure 1 differ with the latitude because images were acquired at different distances. The spatial resolutions in Figure 1 are 350 km 50° – 65° from the equator, 250 km 20° – 50° from the equator, and 110 km within 20° of the equator. We also discuss retrievals of the ammonia (NH_3) volume mixing ratio (VMR) with a relative accuracy of 20% obtained from 4.5- to 5- μm spectroscopy acquired between 25 and 28 August.

3.3. MWR

The six microwave radiometer channels on Juno's MWR experiment [Janssen et al., 2017] scanned close to the perijove subspacecraft longitude (Figure 1c), obtaining observations at each latitude from multiple emission angles. The longitudes of sequential observations at each latitude shifted as a function of time as a result of Jupiter's rotation. Here we examine only nadir or nadir-equivalent data to derive the meridional variability of NH_3 with depth. Figure 1d illustrates a 1.38-cm MWR map. Jupiter's rotation enabled the limited longitudinal sampling, and radiances were converted to their nadir equivalents by using a quadratic fit to all data with emission angles $\leq 50^\circ$ and cubic interpolation across sampling gaps using a 2° grid spacing. Figures 1e–1g

represent nadir-equivalent longitudinally averaged results in 1° latitude bins using data with emission angles $\leq 5^\circ$ for 1.38 cm (channel 6), 3.0 cm (channel 5), and 5.75 cm (channel 4), respectively. We also examine the retrieved NH_3 VMR from MWR observations.

3.4. Ground-Based Imaging

We present a $5.1\text{-}\mu\text{m}$ image from NASA's Infrared Telescope Facility (IRTF) taken with the scientific-grade guide camera of the near-infrared spectrometer SpeX [Rayner *et al.*, 2003]. With Jupiter only 23° from the Sun, the telescope dome and shutter shaded the IRTF's primary mirror from direct sunlight, partially obscuring the primary mirror and increasing the off-Jupiter sky brightness. Absolute calibration was therefore not possible. Figure 1c shows an excerpt from a cylindrical projection of the IRTF image. Atmospheric seeing and diffraction limited the spatial resolution to the equivalent of $\sim 1^\circ$ in latitude or longitude at the equator.

4. Results

Figure 1 presents an overview of observations from all the data sources described above. A comparison between the JunoCam map and the $5\text{-}\mu\text{m}$ JIRAM map reinforces a strong correlation between regions that are dark in the visible and bright at $5\text{ }\mu\text{m}$ and between regions that are visibly bright and faint at $5\text{ }\mu\text{m}$. This verifies a previous rigorous correlation by using high spatial resolution Galileo observations by the Near-Infrared Mapping Spectrometer instrument [Irwin *et al.*, 2001]. In this encounter, prominent dark regions around light-colored ovals correspond to particularly bright peripheries of these features at $5\text{ }\mu\text{m}$. The most prominent of these are the ovals at 38°S , but the correspondence extends down to extremely small spatial scales, such as the ovals with dark peripheries poleward of 40° latitude in either hemisphere, as has been noted in earlier Earth-based observations [de Pater *et al.*, 2010, 2011]; see also the JIRAM study by Sindoni *et al.* [2017]. The dark blue-gray discrete features near 7°N correspond to particularly bright features at $5\text{ }\mu\text{m}$. These are known as $5\text{-}\mu\text{m}$ "hot spots" [Terrile and Westphal, 1977] and another focus of JIRAM study [Grassi *et al.*, 2017]. The correlation of regions with high $5\text{-}\mu\text{m}$ radiance and blue-gray appearance has been well established [Owen and Terrile, 1981]. These regions are characterized as the driest and clearest in Jupiter [Terrile and Westphal, 1977; Ortiz *et al.*, 1998; Fletcher *et al.*, 2016] and are of specific interest because the Galileo Probe descended into one of them [Orton *et al.*, 1996, 1998]. A correlation between Juno measurements of the physical properties of the atmosphere in $5\text{-}\mu\text{m}$ hot spots and the Galileo Probe results is considered an important element of closure in the study of Jupiter's atmosphere, linking independent spacecraft results.

Opacity in the $5\text{-}\mu\text{m}$ window is controlled by the opacity of cloud particles, together with moderate gaseous NH_3 , weaker PH_3 , and faint H_2O absorption [Grassi *et al.*, 2010]. In the absence of substantial cloud coverage in the upper troposphere (e.g., $5\text{-}\mu\text{m}$ hot spots), radiation from this window can be sensitive to pressures as deep as 6 bars, although the average radiation emerges from the 4–5 bar level. It is useful to compare the JIRAM $5\text{ }\mu\text{m}$ maps and the MWR channels 4–6, which are sensitive to gaseous NH_3 absorption in the upper troposphere between the $\sim 0.7\text{-}$ and 5-bar atmospheric pressure levels. This should differentiate between gaseous and particulate opacities, given that the particles have been characterized as submicron in size [e.g., Irwin *et al.*, 2001] and thus unlikely to influence microwave radiation. The $5\text{-}\mu\text{m}$ radiances in Figures 1b and 1c can be compared visually with the limited-area map of MWR radiances in channel 6 (Figure 1d) and a representation of the nadir-equivalent MWR radiances in its channels 4–6 in Figures 1e–1g, respectively.

More quantitatively, Figure 2 compares the MWR brightness temperatures with the brightness temperatures equivalent to convolving radiances in the JIRAM high-resolution map with the MWR channel 6 angular sensitivity function. There is a correlation of bright areas in both spectral regions in the North Equatorial Belt (NEB), which is bright at $5\text{ }\mu\text{m}$ between 7° and 14°N and in the MWR channels between 7° and 15°N – 19°N (depending on the MWR channel), indicating both low cloud opacity and low NH_3 gaseous absorption relative to the rest of the planet. There is a similar correlation of bright regions at $5\text{ }\mu\text{m}$ and MWR channels 4–6 in the 7°S – 27°S South Equatorial Belt (SEB). However, the amplitude of the MWR radiance in the SEB is significantly lower than in the NEB, despite approximately equal $5\text{-}\mu\text{m}$ radiances, and there is only a faint correlation with bright $5\text{-}\mu\text{m}$ radiances near 35°S . Furthermore, there are faint local maxima in the MWR channels near 28°S , the equator, and (in MWR channel 6) at 22°N that do not correspond to any detectable $5\text{-}\mu\text{m}$ brightening. Figure 2 illustrates that the $5\text{-}\mu\text{m}$ radiances correspond roughly to the same brightness

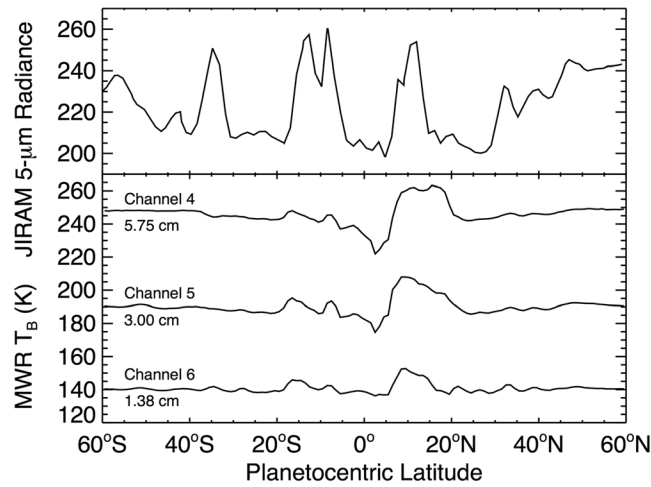


Figure 2. Comparison between (top) JIRAM 5- μm brightness temperatures and (bottom) MWR brightness temperatures. The JIRAM brightness temperatures result from convolving the high-resolution map of the JIRAM radiances shown in Figure 1b, with an angular response function that is an average of the MWR channel, which were then converted to brightness temperatures. The local peak of 5- μm radiance near 11°N latitude corresponds to a discrete feature that is brighter than the zonal mean but less bright than the brightest 5 μm “hot spot.”

[Bjoraker *et al.*, 2015]. It should be stressed, however, that these authors, as well as Giles *et al.* [2016] who analyzed similar high-resolution spectra, explicitly describe a “deep” cloud located between 4 and 5 bars, whereas the opacities derived from the lower resolution JIRAM data most likely refer to higher cloud structures, with effective tops above the 1-bar level. Our data are generally consistent with a standard model of spatial variability in Jupiter’s atmosphere, with “wet” upwelling winds lofting abundant amounts of condensable gas that form clouds, balanced by “dry” regions with downwelling, desiccated cloudless regions. However, we find significant exceptions. The challenge to modeling is to examine all these results together with appropriate radiative-transfer tools.

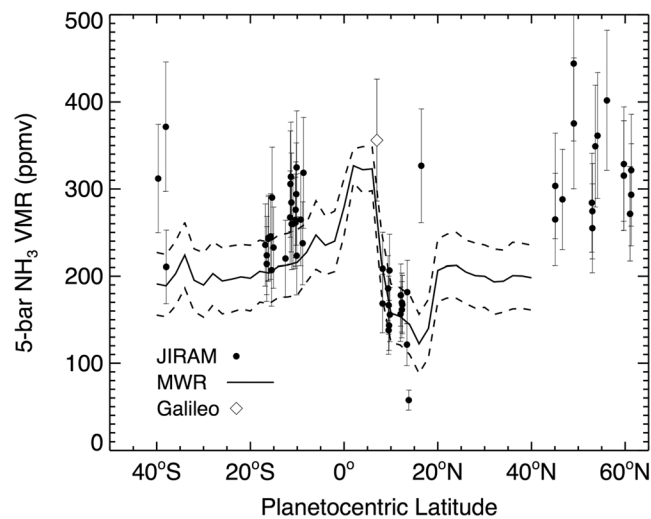


Figure 3. Comparison between retrieved ammonia volume mixing ratio (VMR) from MWR nadir-equivalent radiometry (solid line, with uncertainties denoted by dashed lines) and JIRAM spectroscopy (filled circles, with uncertainties denoted by the vertical error bars). MWR retrievals were not made from latitudes poleward of 40° from the equator to avoid interference from synchrotron radiation. Results from the Galileo Probe relay attenuation signal experiment at this pressure [Folkner *et al.*, 1998; Hanley *et al.*, 2009] are shown by the open diamond and associated uncertainties.

temperatures and thus to the same atmospheric depths, as MWR channels 4 and 5. But the correlation between the brightness at 5- μm brightness and those channels is weak, even accounting for the somewhat larger MWR fields of view. A prominent example of this is the curious depth dependence of the MWR radiances at 5°N–20°N latitudes. The lack of correlation between 5- μm and microwave radiation requires additional opacity arising from particulate opacity at 5 μm . A similar conclusion was reached by de Pater *et al.* [2016] in their mapping of Very Large Array radio emission (illustrated together with MWR observations). Variability of opacity sources among regions appearing relatively bright at 5 μm was noted earlier in high-resolution studies

[Bjoraker *et al.*, 2015]. It should be stressed, however, that these authors, as well as Giles *et al.* [2016] who analyzed similar high-resolution spectra, explicitly describe a “deep” cloud located between 4 and 5 bars, whereas the opacities derived from the lower resolution JIRAM data most likely refer to higher cloud structures, with effective tops above the 1-bar level. Our data are generally consistent with a standard model of spatial variability in Jupiter’s atmosphere, with “wet” upwelling winds lofting abundant amounts of condensable gas that form clouds, balanced by “dry” regions with downwelling, desiccated cloudless regions. However, we find significant exceptions. The challenge to modeling is to examine all these results together with appropriate radiative-transfer tools.

Figure 3 illustrates a start in that direction, comparing determinations of the NH_3 gas at the 5-bar level by both JIRAM and the MWR. JIRAM 4.4–5 μm spectra were analyzed by using a Bayesian retrieval code developed for this purpose [Grassi *et al.*, 2017]. To compare the two data sets, spectra were selected from pixels closest to the MWR track, with longitude adjusted based on average winds derived by Porco *et al.* [2003] and the time elapsed between JIRAM and MWR observations. Then pixels within 1000 km from nominal MWR spots were retained for further analysis. Scatter in the retrievals may therefore reflect imperfect motion compensation

as well as any intrinsic time variability of the atmosphere within the three days of observations. The retrieval code was designed only for relatively bright spectra, thus minimizing the residual contribution of scattered solar radiation and allowing us to assume that nearly all emission is thermal. In these conditions, the JIRAM data provide information on the deep content of ammonia, the relative humidity of water vapor, the mean content of disequilibrium species (phosphine, germane, and arsine), and the opacity of clouds, following the approach of *Grassi et al.* [2010]. For most of the gaseous species, JIRAM sensitivity peaks between ~ 3 and 6 bars; JIRAM retrievals are representative of mean NH_3 abundance around 5 bars. Numerical experiments on simulated observations demonstrated that the *relative* accuracy on retrieved values of ammonia is around 20% and improves to 10% for phosphine and water vapor relative humidity.

Retrievals of the NH_3 volume mixing ratio (VMR) from MWR observations take advantage of the fact that NH_3 is by far the dominant microwave absorber in Jupiter's atmosphere to interpret the microwave spectrum measured at each latitude as due to a vertical distribution of NH_3 concentration, accounting also for the small contributions of $\text{H}_2\text{-H}_2$ collision-induced absorption. Because the meridional variation of brightness temperature (~ 30 K) is much larger than possible temperature variations, a meridionally uniform temperature profile was assumed. The retrievals follow the hybrid approach given by *Li et al.* [2017]. First, the deep ammonia abundance is derived by using the nadir brightness temperatures of the six channels near the equator, assuming that the atmosphere is an ideal moist adiabat, because it is where the brightness temperatures are lowest. Second, using this deep-ammonia abundance, a set of scaling factors were introduced to represent the desiccation of ammonia gas away from the equator. These scaling factors were then retrieved by matching the brightness temperature spectrum latitude by latitude using the Markov chain Monte Carlo retrieval algorithm. The uncertainty in the NH_3 absorption coefficient plus reasonable uncertainties involving model assumptions for atmospheric composition and temperature lapse rate combine to give a net uncertainty of about 20% in the concentration. The NH_3 VMR was found to vary more than 50% in both depth and latitude, from an asymptotic maximum of 360 ppmv at pressure levels below 50–100 bar to values varying from 120 ppmv to 320 ppmv around the 5-bar level.

Figure 3 shows that, as a whole, the retrieved values from MWR and JIRAM are remarkably self-consistent within their assigned uncertainties, including estimates of the systematic sources of absolute radiometric uncertainty. The few outliers among the JIRAM retrievals, both above and below the MWR results, could arise from errors in the extrapolation of the mean zonal flow used to correct the positions of the retrieval locations to points along the MWR track, e.g., if the flow at the 5-bar level of these retrievals is significantly different from the flow obtained by visible feature tracking [*Porco et al.*, 2003]. Otherwise values for the NH_3 VMR derived from JIRAM spectra might differ from the MWR values due to ambiguity in differentiating between gaseous NH_3 and otherwise unknown absorption or particulate scattering. Nevertheless, the overall consistency of the results provides confidence in this part of the retrieval process that includes the 5-bar region. Overlapping results at 5 bars between 8°N and 9°N , averaging 197 ± 46 ppmv (considering sampling error and absolute uncertainties) are nominally lower than the $\sim 356 \pm 70$ ppmv derived from the Galileo Probe signal-attenuation experiment by *Folkner et al.* [1998], with opacity corrections from *Hanley et al.* [2009] (see *Wong et al.* [2004] for a summary). The 5-bar MWR results indicate a steep rise with decreasing latitude and a value of 306 ± 30 ppmv closer to the Galileo Probe entry latitude of 6.7°N [*Young et al.*, 1996], yielding overlapping uncertainties with the Galileo results (Figure 3). Verifying the relatively high values for the NH_3 VMR derived by JIRAM poleward of 40°N by using MWR measurements awaits further analysis.

Finally, we compare the deep NH_3 meridional variability derived from the MWR with other gases that are commonly used as indirect indicators of vertical motions. Figure 4a shows the 33-bar NH_3 VMR retrieved from MWR observations by *Li et al.* [2017]. This level is the deepest true tie point that was retrieved in their analysis, with values interpolated between 33 bars and 100 bars, where meridionally uniform VMR was assumed. The uncertainties shown represent absolute uncertainties in the derived values, with relative uncertainties in the latitudinal variability being an order of magnitude smaller. The ammonia abundance at depth is concentrated in a narrow band within 20° latitude of the equator [*Li et al.*, 2017], with the JIRAM results suggesting a greater abundance toward higher latitudes. Using NH_3 as a condensate tracer, this is consistent with substantial convection of saturated air from great depth, with the possibility of weaker convection increasing from equator to pole. The derived deep ammonia abundance is consistent with the lower limit of the Galileo Probe uncertainty for the mass spectrometer data [*Wong et al.*, 2004] but lower than that from radio

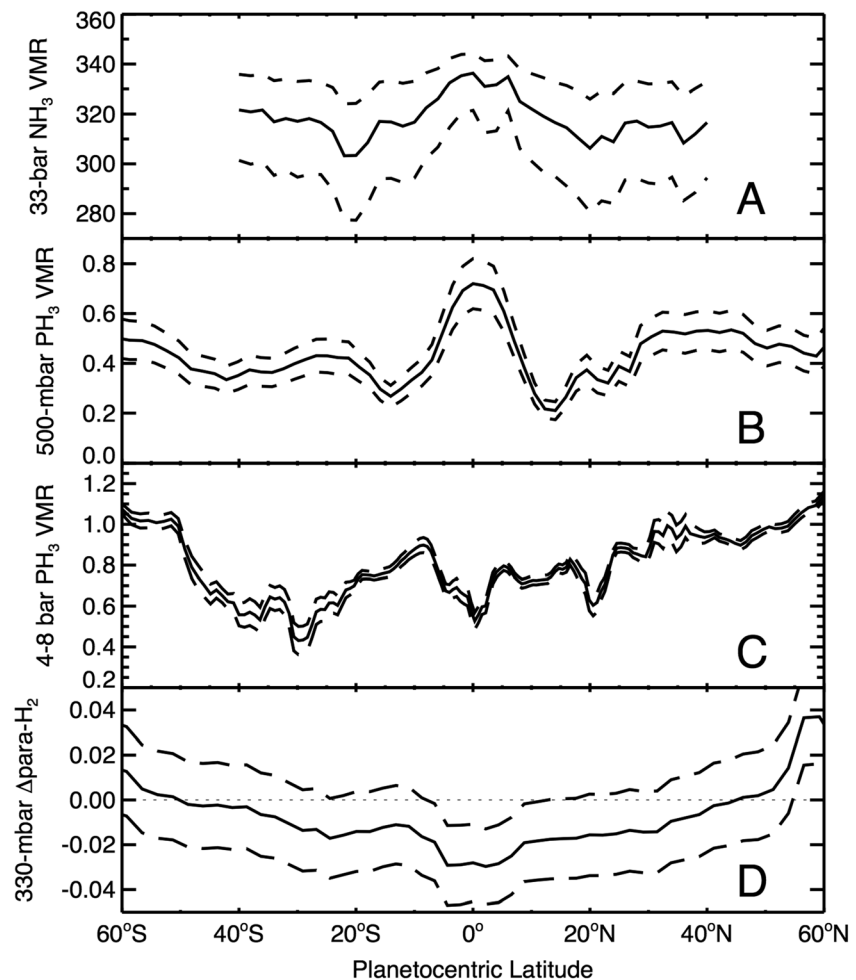


Figure 4. Comparison between the 33-bar NH_3 abundance in ppmv derived by *Li et al.* [2017] from (a) Juno MWR radiometry and other indirect tracers of vertical motions. (b) The 500-mbar PH_3 VMR (ppmv) derived from a reanalysis of 2001 Cassini CIRS data by *Fletcher et al.* [2016]. (c) The ~5-bar PH_3 VMR (ppmv) from the analysis of 2012–2013 Very Large Telescope CRIRES observations by *Giles et al.* [2016]. (d) The 330-mbar para- H_2 fraction difference from its equilibrium value derived from 1979 Voyager 1 IRIS data by *Fletcher et al.* [2017]. Relative (latitude-to-latitude) uncertainties in the derived quantities are shown by the dashed curves, except Figure 4a, which displays absolute-radiance uncertainties.

attenuation data [*Folkner et al.*, 1998], noting that the probe sampled a single meteorologically anomalous location down to 22 bars.

Other tracers that have been discussed include disequilibrium species, such as PH_3 , AsH_3 , and GeH_3 , all detected at the several-bar pressure level or higher, despite being thermochemically unstable at those levels. They are presumed to be present there because of rapid convection from their thermochemical equilibrium level (≥ 1000 K, ≥ 1 kbar) to upper troposphere [e.g., *Barshay and Lewis*, 1978] without being destroyed along the way. Phosphine has been detected in the upper troposphere by using mid-infrared spectroscopy. *Fletcher et al.* [2017] derived the PH_3 abundance at 500 mbar from Cassini CIRS observations, whose meridional variation (Figure 4b) is strikingly similar to the 33-bar NH_3 abundance (Figure 4a): a central maximum surrounded by a minimum $\sim 15^\circ$ from the equator and a slow drift toward higher abundances at higher latitudes. These retrievals and the 5-bar NH_3 abundance (Figure 3) comprise a consistent story: vigorous convection near the equator is implied by both the relatively high abundance of a condensable at 5 and 33 bars and a disequilibrium constituent at 500 mbar, with weaker convection increasing toward the poles. However, the retrievals of PH_3 at 5 bars from the 5- μm region by *Giles et al.* [2016] show a similar increase toward the poles but no prominent central peak. They retrieve AsH_3 abundances, which also have a strong equator-to-pole increase without a central peak, and GeH_4 abundances, which exhibit an equator-to-pole increase but overlay with

substantial belt-zone variability. They caution that their results contain an implicit degeneracy between gaseous versus cloud opacity. Although this would easily explain belt-zone variability, it is unclear whether it could also be responsible for the difference between PH₃ abundances at 5 bars and 500 mbar. This difference remains an issue for further investigation. Finally, we consider the para-H₂ versus ortho-H₂ ratio, which is known to vary meridionally from its equilibrium value, also presumed to arise from replenishment from deeper, warmer levels due to upwelling and higher, colder areas due to subsidence that is meridionally variable [Conrath and Gierasch, 1984]. Para-H₂ fractions lower than local equilibrium values indicate consistency with equilibrium at higher than ambient temperatures. Thus, the central drop of the 330-mbar para-H₂ close to the equator (Figure 4d) is consistent with a model of upward convection there. Its rise toward higher latitudes would be consistent with increasing downward convection if dynamics alone were responsible. Fletcher *et al.* [2017] point out that, besides a dynamical explanation, interconversion of para-H₂ and ortho-H₂ on the surfaces of stratospheric aerosols could be equally responsible, particularly at very high latitudes, where the number density of these aerosols is known to increase [Zhang *et al.*, 2013].

5. Conclusions

Comparison of observations of Jupiter's atmosphere by Juno's remote-sensing instruments verified a significant correlation between regions with visibly dark clouds and high 5- μm brightness, regions with low cloud opacity, or low ammonia gas abundance. Dark regions are also correlated with low ammonia abundance in the 5–33 bar range derived from microwave mapping. However, there are also significant exceptions that are most likely due to additional small-particulate opacity at 5 μm to which microwave radiation is insensitive. Despite the exceptions, a model is generally valid with rising gas producing high abundances of saturated condensates that form clouds with abundant particulate populations and downwelling air producing desiccated, cloudless conditions. Measurements of the 5-bar gaseous NH₃ abundance from 5- μm JIRAM spectroscopy and MWR radiometry are generally consistent with each other over a wide latitude range. They are consistent with NH₃ at the lower range of uncertainty of the Galileo probe-relay attenuation results. The high abundance of NH₃ near the equator, measured by the MWR over a broad vertical region, is consistent with vigorous convection and is reflected in the meridional distribution of para-H₂ near 330 mbar and PH₃ at 500 mbar by studies of midinfrared emission. The absence of such a signature in the meridional distribution of PH₃ near the ~5-bar level might arise from an implicit degeneracy between PH₃ and cloud opacity in the analysis of the 5- μm spectroscopy. A slower rise in the 5-bar NH₃ abundance toward higher latitudes is suggested by 5- μm and microwave results. It is consistent with a picture of gradually increasing strength of upwelling circulation toward the poles, reflected in the general rise of other indirect indicators of upwelling in the troposphere—the increase of disequilibrium species abundances (PH₃, AsH₃, and GeH₄) with latitude. This picture is inconsistent with a dynamical explanation for the slow rise of para-H₂ at the 330-mbar level with latitude, but the para-H₂ rise could instead be the result of more efficient interconversion between para-H₂ and ortho-H₂ states on haze particles whose abundance increases with increasing latitude.

Acknowledgments

A substantial portion of this research was funded by the National Aeronautics and Space Administration through the Juno Project; some of these funds were distributed to the Jet Propulsion Laboratory, California Institute of Technology. The development of JIRAM and the work of Italian coauthors were supported by the Italian Space Agency through ASI-INAF contract I/010/10/0 and 2014-050-R.O. J. G. We are grateful to Leigh Fletcher and to Rohini Giles for numerical versions of their results shown in Figure 4. All JunoCam images can be obtained on the Mission Juno Web site (<https://www.missionjuno.swri.edu>).

References

- Adriani, A., *et al.* (2014), JIRAM, the Jovian Infrared Auroral Mapper, *Space Sci. Rev.*, doi:10.1007/s11214-014-0094-y.
- Barshay, S. S., and J. S. Lewis (1978), Chemical structure of the deep atmosphere of Jupiter, *Icarus*, 33, 593–611.
- Bjoraker, G. L., M. H. Wong, I. de Pater, and M. Ádámkóvics (2015), Jupiter's deep cloud structure revealed using Keck observations of spectrally resolved line shapes, *Astrophys. J.*, 810(2), 122, doi:10.1088/0004-637X810/2/122.
- Conrath, B. J., and P. J. Gierasch (1984), Global variation of the para-hydrogen fraction in Jupiter's atmosphere and implications for the dynamics on the outer planets, *Icarus*, 54, 187–204, doi:10.1016/0019-1035(84)90065-4.
- de Pater, I., M. Wong, K. de Kleer, P. Marcus, S. Luszcz-Cook, M. Ádámkóvics, A. Conrad, X. Asay-Davis, and C. Go (2010), Persistent rings in and around Jupiter's anticyclones—Observations and theory, *Icarus*, 210(2), 742–762, doi:10.1016/j.icarus.2010-07.027.
- de Pater, I., M. H. Wong, K. de Kleer, H. B. Hammel, M. Ádámkóvics, and A. Conrad (2011), Keck adaptive optics images of Jupiter's north polar cap and Northern Red Oval, *Icarus*, 213(2), 559–563, doi:10.1016/j.icarus.2011.03.006.
- de Pater, I., R. J. Sault, B. Butler, D. DeBoer, and M. H. Wong (2016), Peering through Jupiter's clouds with radio spectral imaging, *Science*, 352(6290), 1198–1201.
- Fletcher, L. N., T. K. Greathouse, G. S. Orton, J. A. Sinclair, R. S. Giles, P. G. J. Irwin, and T. Encrenaz (2016), Mid-infrared mapping of Jupiter's temperatures, aerosol opacity and chemical distributions with IRTF/TEXES, *Icarus*, 278, 128–161, doi:10.1016/j.icarus.2016.06.008.
- Fletcher, L. N., I. de Pater, W. T. Reach, M. Wong, G. S. Orton, P. G. J. Irwin, and R. D. Gehrz (2017), Jupiter's para-H₂ distribution from SOFIA/FORCAST and Voyager/IRIS 17–37 μm spectroscopy, *Icarus*, 286, 223–240, doi:10.1016/j.icarus.2016.10.002.
- Folkner, W. M., R. Woo, and S. Nandi (1998), Ammonia abundance in Jupiter's atmosphere derived from attenuation of the Galileo probe's radio signal, *J. Geophys. Res.*, 103, 22,847–22,856, doi:10.1029/98JE01635.

- Giles, R. S., L. N. Fletcher, and P. G. J. Irwin (2016), Latitudinal variability in Jupiter's tropospheric disequilibrium species: Ge₄, AsH₃ and PH₃, *Icarus*, doi:10.1016/j.icarus.2016.10.023.
- Grassi, D., et al. (2010), Jupiter's hot spots: Quantitative assessment of the retrieval capabilities of future IR spectro-images, *Planet. Space Sci.*, 58(10), 1265–1278, doi:10.1016/j.pss.2010.05.003.
- Grassi, D., et al. (2017), Preliminary results on the composition of Jupiter's troposphere in hot spot regions from the JIRAM/Juno instrument, *Geophys. Res. Lett.*, doi:10.1002/2017GL072841, in press.
- Hanley, T. R., P. G. Steffes, and B. M. Karpowicz (2009), A new model of the hydrogen and helium-broadened microwave opacity of ammonia based on extensive laboratory measurements, *Icarus*, 202(1), 316–335, doi:10.1016/j.icarus.2009.02.002.
- Hansen, C. J., M. A. Caplinger, A. Ingersoll, M. A. Ravine, E. Jensen, S. Bolton, and G. Orton (2014), Junocam: Juno's outreach camera, *Space Sci. Rev.*, doi:10.1007/s11214-014-0079-x.
- Irwin, P. G. J., A. L. Weir, F. W. Taylor, S. B. Calcutt, and R. W. Carlson (2001), The origin of belt/zone contrasts in the atmosphere of Jupiter and their correlation with 5- μ m opacity, *Icarus*, 149, 397–415, doi:10.1006/icar.2000.6542.
- Janssen, M. A., et al. (2017), MWR: Microwave Radiometer for the Juno mission to Jupiter, *Space Sci. Rev.*, doi:10.1007/s11214-017-0349-5.
- Li, C., A. P. Ingersoll, S. Ewald, F. Oyafuso, and M. Janssen (2017), Jupiter's global ammonia distribution from inversion of Juno Microwave Radiometer observations, *Geophys. Res. Lett.*, doi:10.1002/2017GL073159, in press.
- Ortiz, J. L., G. S. Orton, A. J. Friedson, S. T. Stewart, B. M. Fisher, and J. R. Spencer (1998), Evolution and persistence of 5- μ m hot spots at the Galileo Probe entry latitude, *J. Geophys. Res.*, 103, 23,051–23,069, doi:10.1029/98JE00696.
- Orton, G., et al. (1996), Results of Earth-based observations of the Galileo Probe entry site, *Science*, 272, 839–840.
- Orton, G. S., et al. (1998), Characteristics of the Galileo Probe entry site from Earth-based remote sensing observations, *J. Geophys. Res.*, 103, 22,791–22,814, doi:10.1029/98JE02380.
- Owen, T., and R. J. Terrile (1981), Colors on Jupiter, *J. Geophys. Res.*, 86, 8797–8814, doi:10.1029/JA086iA10p08797.
- Porco, C., et al. (2003), Cassini imaging of Jupiter's atmosphere, satellites, and rings, *Science*, 299, 1541–1547.
- Rayner, J. T., D. W. Toomey, P. M. Onaka, A. J. Denault, W. E. Stahlberger, W. D. Vacca, M. C. Cushing, and S. Wang (2003), SpeX: A medium-resolution 0.8–5.5 micron spectrograph and imager for the NASA Infrared Telescope Facility, *Pub. Astron. Soc. Pacific*, 115, 362–382.
- Sindoni, G., et al. (2017), Characterization of the white ovals on the Jupiter's southern hemisphere using the first data by Juno/JIRAM instrument, *Geophys. Res. Lett.* doi:10.1002/2017GL072940, in press.
- Terrile, R. J., and J. A. Westphal (1977), The vertical cloud structure of Jupiter from 5 micron measurements, *Icarus*, 30, 274–281, doi:10.1016/0019-1035(77)90159-2.
- Wong, M. H., P. R. Mahaffy, S. K. Atreya, H. B. Niemann, and T. C. Owen (2004), Updated Galileo Probe mass spectrometer measurements of carbon, oxygen, nitrogen, and sulfur on Jupiter, *Icarus*, 171(1), 153–170, doi:10.1016/j.icarus.2004.04.010.
- Young, R. E., M. A. Smith, and S. K. Sobeck (1996), Galileo Probe: In situ observations of Jupiter's atmosphere, *Science*, 272, 837–838.
- Zhang, X., R. A. West, D. Banfield, and Y. L. Yung (2013), Stratospheric aerosols on Jupiter from Cassini observations, *Icarus*, 226, 159–171, doi:10.1016/j.icarus.2013.05.020.